Tailoring the surface and interface states in a three-dimensional fragile topological insulator with kagome lattice

Boyang Xie,[1,*] Hui Liu,[1,*] Haonan Wang,[1] Hua Cheng,[1,†] Jianguo Tian,[1,‡] Zhengyou Liu,[2] and Shuqi Chen ●[1,3,4,§]

[1]*The Key Laboratory of Weak Light Nonlinear Photonics, Ministry of Education,*
Renewable Energy Conversion and Storage Center, School of Physics, and TEDA Institute of Applied Physics,
Nankai University, Tianjin 300071, China
[2]*Key Laboratory of Artificial Micro- and Nanostructures of Ministry of Education and School of Physics and Technology,*
Wuhan University, Wuhan 430072, China
[3]*The Collaborative Innovation Center of Extreme Optics, Shanxi University, Taiyuan, Shanxi 030006, China*
[4]*Collaborative Innovation Center of Light Manipulations and Applications, Shandong Normal University, Jinan 250358, China*

Topological insulators, which are insulating in the bulk and conducting on the surface, have attracted great interest in recent years. The recently discovered topological surface and hinge states in three dimensions have provided promising methods for wave manipulation in classical systems. However, the combination of surface states and interface states has yet to be achieved in phononic crystals due to the missing topological surface states. Here, we experimentally demonstrate a fragile topological insulator with a bilayer kagome lattice. We observe the surface states in three different orientations and interface states formed by inversion of layer pseudospin sectors or bands. The combination of surface and interface states is investigated in X-shaped waveguides. Our work may provide a platform for exploring unique acoustic applications based on surface or interface states.

I. INTRODUCTION

Topological insulators that support robust energy transport in the presence of disorder and defects have attracted great interest in condensed-matter physics and have been extended to photonics [1–6], acoustics [7–10], and mechanics [11,12]. They have shown great potential for applications in two-dimensional (2D) systems such as robust waveguides, splitters, lasers [13], and directional antennas [14]. One way of generating topological effects is based on the analogy to fermionic time-reversal symmetry and spin-orbit coupling. In 2D acoustic topological insulators, fermionic time-reversal symmetry is provided by crystal symmetry, which behaves in the same way as time-reversal symmetry in electronic systems and renders the Kramers doubling. Pseudospin up and down are defined corresponding to positive and negative angular momenta of the wave function. The implementation of pseudospin was realized using acoustic scatterers [7,15] and coupled waveguides [16]. Beyond purely 2D structures, bilayer spin-Chern structures implement pseudospin by defining layer pseudospin up and down for the upper and lower layers [9,17]. The bands below the band gap can be projected in two spin sectors which carry opposite spin-Chern numbers. As they require neither any symmetry nor the presence of a fermionic time-reversal operator, they can realize helical edge

states on the boundaries or surfaces. Recent research has also observed spectral flow under twisted boundary conditions in the bilayer system as a signature of the fragile topology defined by the theory of topological quantum chemistry [18,19]. Fragile topological bands can be trivialized by a set of bands arising from an atomic limit, which challenges the conventional notion of topological robustness.

The research on topological acoustics in three-dimensional (3D) structures first focused on topological semimetals, including the research on Weyl points [20–22], 3D Dirac points [23–25], nodal lines [26,27], and nodal surfaces [28]. Breaking the symmetry in topological semimetals can give rise to topological gaps in three dimensions. In particular, 3D topological insulators can be achieved by breaking the spatial symmetry in 3D Dirac materials [29,30]. While 2D topological insulators host one-dimensional (1D) topological edge states and zero-dimensional (0D) corner states, 3D topological insulators can exhibit 2D topological surface states, 1D hinge states, and 0D corner states. Although the topological crystalline insulators in photonic systems differs from the "strong" and "weak" topological insulators in electric systems, the analogs of weak topological insulators have been realized with dielectric metamaterials [31] and 3D arrays of metallic split-ring resonators [32]. Acoustic analogs of weak topological insulators have been realized with bilayer chiral structures [33], where hinge states were further achieved through Kekulé distortion. The appearance of 2D Dirac cones in the domain wall is typical in these classical systems. However, the helical surface states on the side surfaces were not taken into account in acoustic or photonic 3D topological insulators. Here, the surface states are formed with a hard

---

*These authors contributed equally to this work.
†Corresponding author: hcheng@nankai.edu.cn
‡Corresponding author: jjtian@nankai.edu.cn
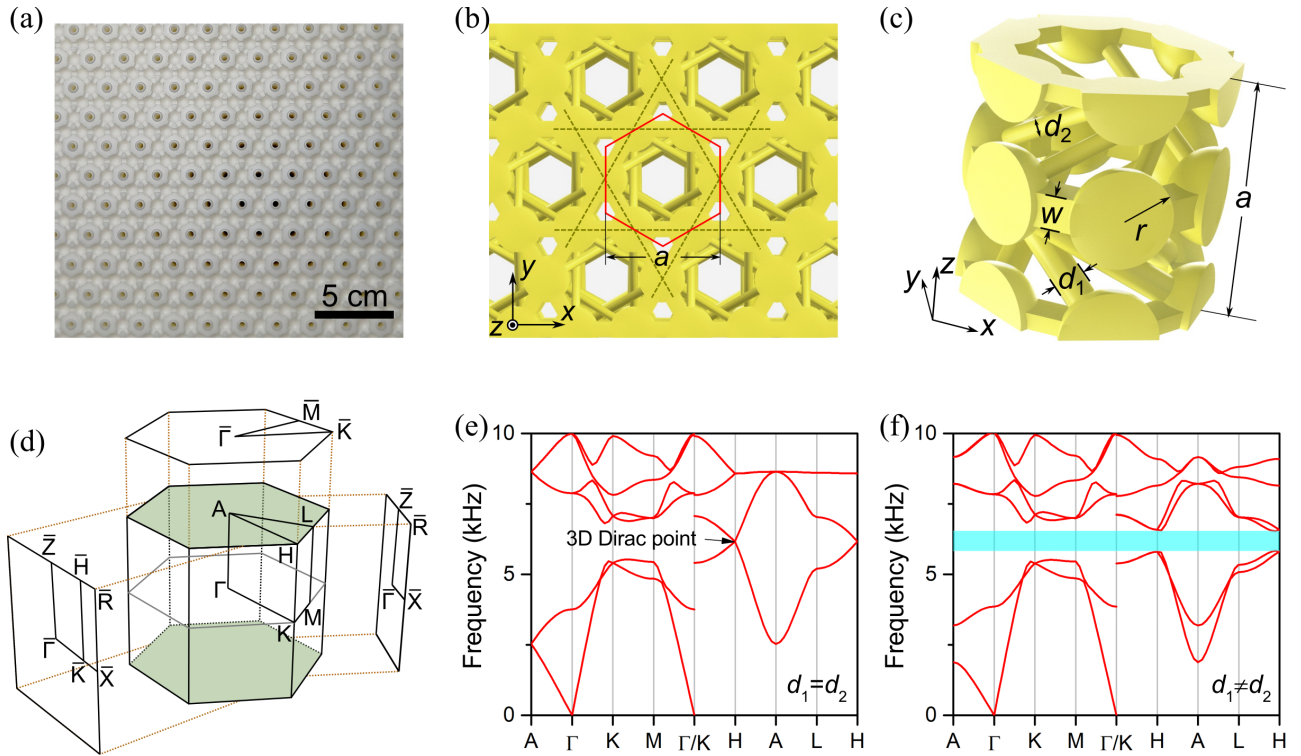§Corresponding author: schen@nankai.edu.cn

FIG. 1. (a) Photo of the acoustic fragile topological insulator. (b) Top view and (c) unit cell of a kagome lattice as the complement structure of (a). The kagome structure is demonstrated by dashed lines connecting the centers of cavities in (b). The structure parameters are $a = 22$ mm, $r = 4.4$ mm, $d_1 = 1.65$ mm, $d_2 = 2.75$ mm, and $w = 3.03$ mm. (d) BZ for the unit cell. (e) Simulated band dispersion of the acoustic crystal. A 3D Dirac point is formed when $d_1 = d_2$. Here, $d_1 = d_2 = 2.2$ mm. (f) Simulated dispersion of the acoustic topological insulator. The blue region represents the complete topological band gap.

boundary, which is distinct from the interface states on the interface or domain wall between two crystals. The role of the fragile topology in forming the surface or interface states in 3D topological insulators is unclear. The transport behavior between the surface and interface has not yet been explored.

In this work, we report a 3D acoustic topological insulator consisting of a bilayer kagome lattice. By tuning the interlayer coupling, a full acoustic band gap is created by lifting the 3D Dirac degeneracy. We demonstrate the appearance of surface states confined to the hard boundaries and interface states confined to the domain wall between two topologically distinct acoustic crystals. Surface states are observed in three different orientations, in which the surface states at the side surfaces are layer pseudospin polarized. Various kinds of interface states are achieved by tuning the interlayer hopping strength and chiralities. The mechanism behind the interface states is the inversion of pseudospin sectors or bands. The layer-pseudospin-polarized surface or interface states beyond the band inversion mechanism were not covered in previous works. We focus on the interaction between the surface and interface states in X-shaped waveguides. By combining these topological states, acoustic wave propagation can be manipulated in a variety of different ways.

II. MODEL AND METHODS

The acoustic crystal shown in Fig. 1(a) is fabricated by 3D printing acoustically hard walls around the air volume

shown in Figs. 1(b) and 1(c). The Brillouin zone (BZ) of the unit cell is shown in Fig. 1(d). The acoustic crystal has $25 \times 13 \times 15$ periods in the x, y, and z directions. The acoustic crystal has an AA stacking of cavities in a kagome lattice, connected by air channels with alternating chiralities and hopping strength. The air channels between layers are cylindrical tubes with diameters d_1 and d_2. We obtained the simulated results using finite-element methods (COMSOL MULTIPHYSICS), with a density of air of 1.2 kg/m^3 and a velocity of airborne sound of 343 m/s. When $d_1 = d_2$, the acoustic system is a type-I Dirac sonic crystal. The 3D Dirac point emerging at the BZ corner is protected by two glide reflections and C_{3v} symmetry. Each glide reflection involves a half translation along the rotation axis: $G_x = \{M_x | (a/2)\hat{z}\}$ and $G_y = \{M_y | (a/2)\hat{z}\}$. The C_{3v} symmetry gives rise to nodal lines that are doubly degenerate at KH or $K'H'$ of the BZ. The glide reflections force the nodal lines to cross and form a 3D Dirac point at H of the BZ. When $d_1 \neq d_2$, the glide reflection and mirror symmetries are broken, which lifts the 3D Dirac cone to a topological complete band gap (5.84 to 6.54 kHz, 11.3% relative band gap width), as shown in Figs. 1(e) and 1(f). The lifting of the Dirac cone can contribute to an effective mass $m = 2(t_{c1} - t_{c2})$, where t_{c1} and t_{c2} are the hoppings between layers, corresponding to tubes of diameters d_1 and d_2. Band inversion occurs at the H point of the BZ when the effective mass changes sign. The tight-binding model analysis using the $\mathbf{k} \cdot \mathbf{P}$ perturbation method is given in Appendices A 1 and A 3.
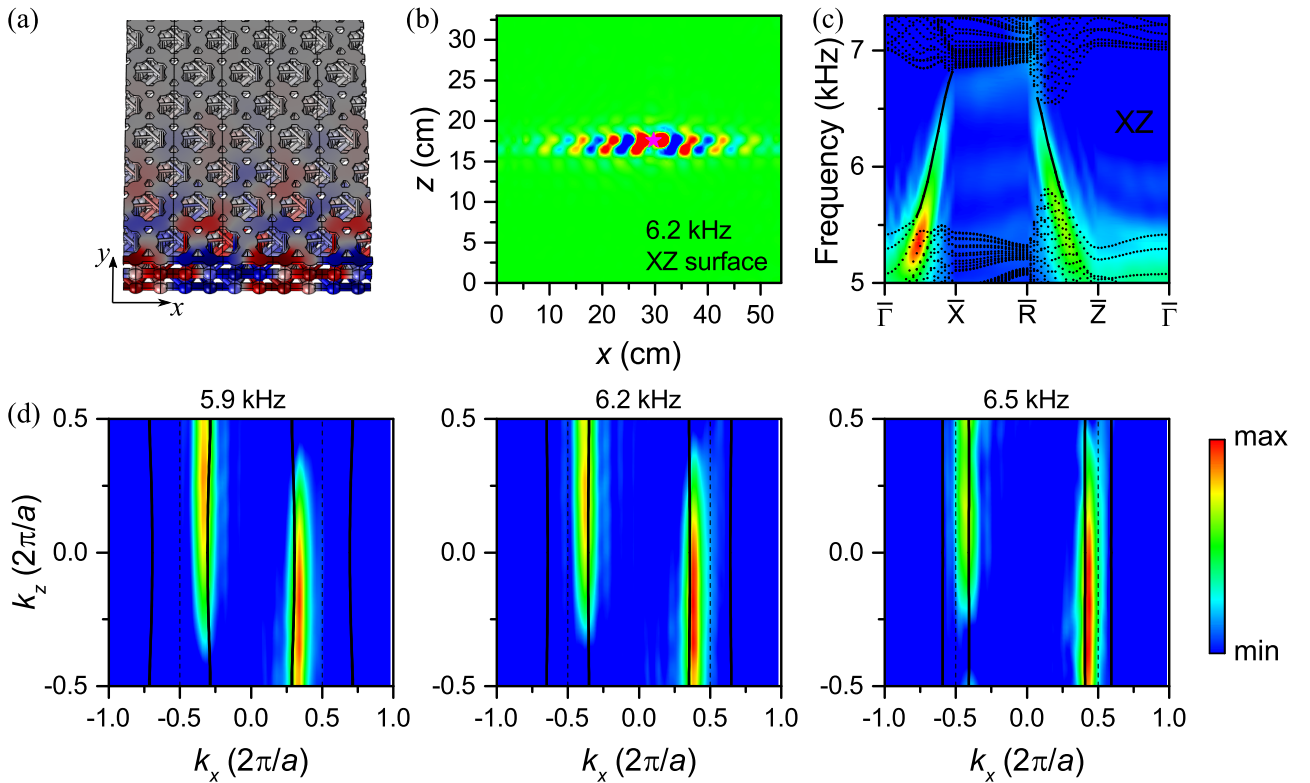
FIG. 2. (a) Simulated pressure field distribution of the topological surface state on the (a) XZ (100) surface with a flat boundary. (b) Measured real-space propagation of a surface wave excited by a pointlike source. (c) Surface band dispersion on the XZ surface. (d) Equifrequency contours of the surface state at 5.9, 6.2, and 6.5 kHz. The color bar in (c) and (d) denotes the magnitude of the spatial Fourier transformation. The black lines and dots denote the simulation results. The dashed black lines denote the boundary of the first BZ.

The fragile topology is based on the fact that the band topology in fragile topological phases is weaker than that in stable topological phases captured within K-theory because the Wannier-obstructed fragile bands can be explicitly trivialized by the presence of an additional atomic insulator. According to topological quantum chemistry, an isolated orbital at a high-symmetry point in real space induces a corresponding combination of bands in the reciprocal space, which is called the elementary band representation (EBR). The classification of the crystalline insulator is turned into the matching between possible EBRs and the bands in the material. If the bands can be written as a combination of EBRs, the crystal is an atomic insulator. Otherwise, EBRs can be decomposed with fractional coefficients for a stable topological insulator or decomposed with integer positive and negative coefficients for a fragile topological insulator. It was shown that the fragile topology has experimental signatures at the boundary according to the twisted bulk-boundary correspondence. Recently, gapless surface states were found in fragile topological insulators protected by rotation symmetry [34], although the fragile phases generally do not exhibit gapless surface states, in contrast to the stable phases. The acoustic crystal is a fragile topological insulator, as the lowest two bands have a missing EBR induced by the Wyckoff position (see Appendix A 2 for details). In our work, we discuss the mechanisms of surface or interface states in an acoustic fragile insulator. For each k_z, the winding of Wannier centers is nontrivial. As the acoustic crystal is obtain by stacking the

spin-Chern insulator with appropriate interlayer couplings, the two bands below the band gap can be projected into layer pseudospin sectors which have nontrivial spin-Chern number $C_s = 1$ on each k_z plane [17]. If the chirality of the interlayer hopping is inverted, the spin-Chern number will change sign. Because the lowest two bands are fragile, the occurrence of surface or interface states does not rely on the band inversion mechanism, which is often used to generate interface states in obstructed atomic insulators. In the next section, we demonstrate how the surface or interface states arise from the bulk topology.

III. SURFACE AND INTERFACE STATES

The topological surface states of the acoustic crystal are shown in Fig. 2. A robust pseudospin wave is generated at the side surfaces due to the nontrivial spin-Chern number and nontrivial winding of the Wannier centers. The layer pseudospins up and down for surface states can be defined with the projection on σ_y (see Appendix A 2 for details). We obtain two branches of surface states with pseudospin-momentum locking: the branch of $\langle \sigma_y \rangle > 0$ is counterclockwise transporting (see above) within $k_x \in (0, \pi/a)$ in the surface BZ, and the branch of $\langle \sigma_y \rangle < 0$ is clockwise transporting within $k_x \in (-\pi/a, 0)$, which is the time-reversal counterpart of the branch of $\langle \sigma_y \rangle > 0$. When the chirality of interlayer hopping is inverted, the sign of $\langle \sigma_y \rangle$ switches, accompanied by the inversion of pseudospin-polarized sectors. The pressure field
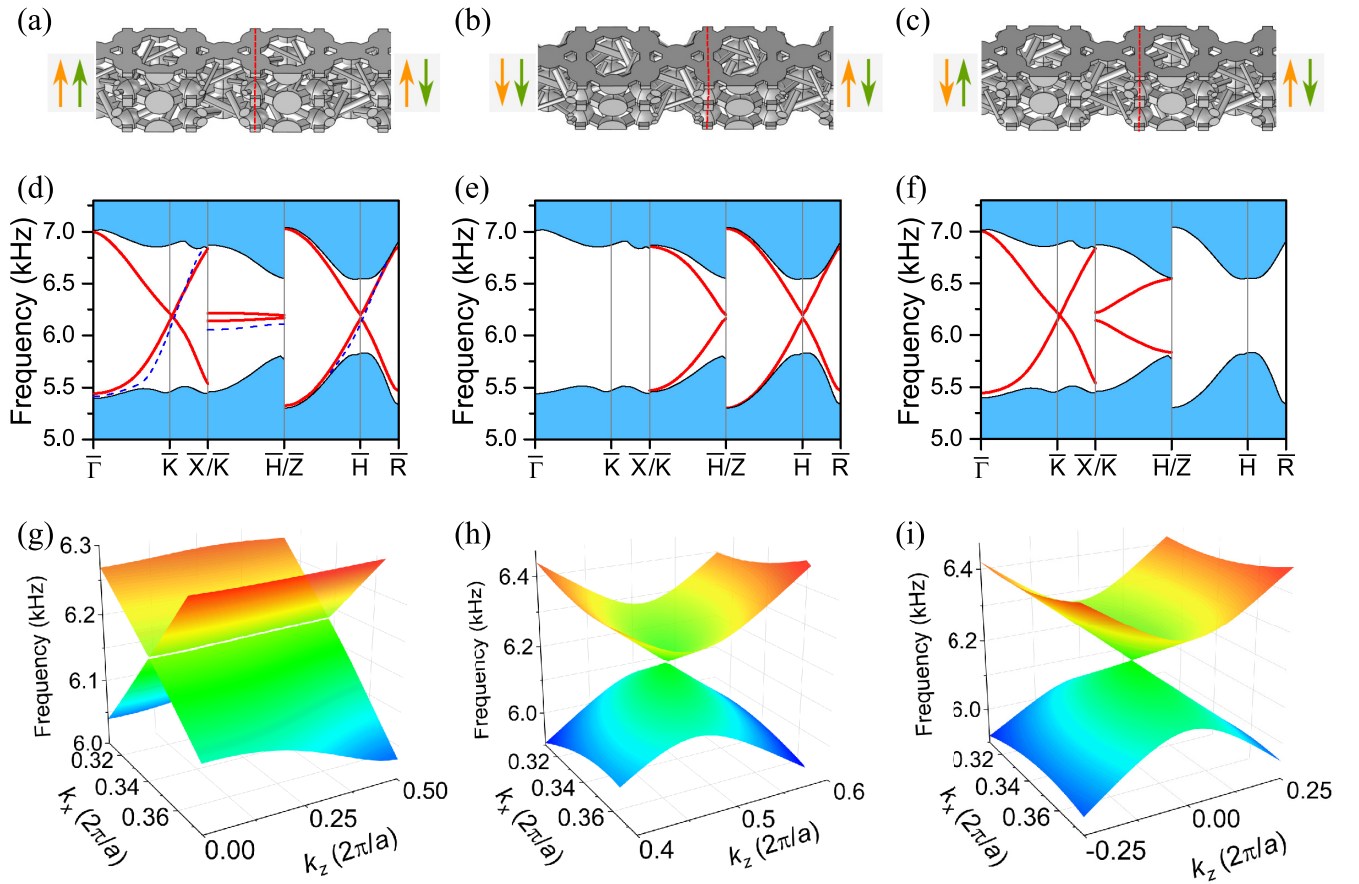
FIG. 3. (a) Interface formed by inverting the chirality of interlayer hopping. (b) Interface formed by interchanging the interlayer strengths t_{c1} and t_{c2}. (c) Interface formed by interchanging the interlayer hopping strengths and inverting the chirality of the interlayer hopping. The red dashed lines denote the domain wall. Orange up and down arrows represent interlayer hopping strengths $|t_{c1}| > |t_{c2}|$ and $|t_{c1}| < |t_{c2}|$. Green arrows represent the chiralities of interlayer hopping. (d)–(f) Simulated interface band dispersion (red solid line) along the high-symmetry line of the BZ for the interfaces in (a)–(c). The surface band dispersion (blue dashed line) with a hard boundary condition is shown as a reference in (d). (g)–(i) Three-dimensional view of simulated interface dispersion for the interfaces in (a)–(c). The dispersion of the interface in (d) and (g) forms a quasi-1D crossing. An interface Dirac cone appears near the $\bar{H}$ point in (e) and (h) and the $\bar{K}$ point in (f) and (i).

of the $\langle \sigma_y \rangle > 0$ branch is illustrated in Fig. 2(a). The XZ surface has a flat whole-cell boundary. The cavities near the boundary have a smaller radius of $r_b = 3.3$ mm to avoid band crossing between surface states. In the experiment, a pointlike source is inserted into the middle of the surface. A microphone (B&K 4138) is inserted into the sample to obtain the acoustic field signal. A vector network analyzer (Keysight E5061) is used to extract the amplitude and phase profiles of the acoustic waves. The spatial fields in Fig. 2(b) show the propagating acoustic wave measured at 6.2 kHz. The surface waves propagate along the horizontal direction without broadening, which manifests the collimation effect of the acoustic wave. The surface band information can be obtained by Fourier transforming the measured field. The measured band dispersions on the XZ surface are shown in Fig. 2(c). There is a pair of surface bands under time-reversal symmetry in the surface BZ. The equifrequency contours for the XZ surface are almost flat, as shown in Fig. 2(d), which agrees with the measured spatial field distribution. Similar surface states on the YZ surface with a zigzag boundary are shown in Appendix B.

In addition to the layer-pseudospin-polarized surface states, we can realize interface states that are also layer pseudospin polarized. The interface is formed by inverting the chirality of the interlayer hopping, as shown in Fig. 3(a). The interface bands form a quasi-1D crossing at each k_z as two pseudospin-polarized interface states cross each other, as shown in Figs. 3(d) and 3(g). The number of interface states is doubled compared to the surface states because the difference of pseudospin-Chern number is doubled between the domains.

To create an interface Dirac cone in the acoustic system, an interface with band inversion should be introduced (see Sec. A 3 for details). By exchanging the interlayer hopping strengths t_{c1} and t_{c2} [see Fig. 3(b)], an inversion between the two lowest bands and two upper bands can occur at H in the BZ, as shown in Figs. 3(e) and 3(h).

Now we have demonstrated two different mechanisms for the interface states, with or without band inversion. It would be very interesting to see how these mechanisms combine. Figure 3(c) shows the interface formed with inverted chirality and exchanged interlayer hopping strengths. A surface Dirac cone is observed at $(k_x, k_z) = (0.3437, 0) \times 2\pi/a$ near $\bar{K}$, as
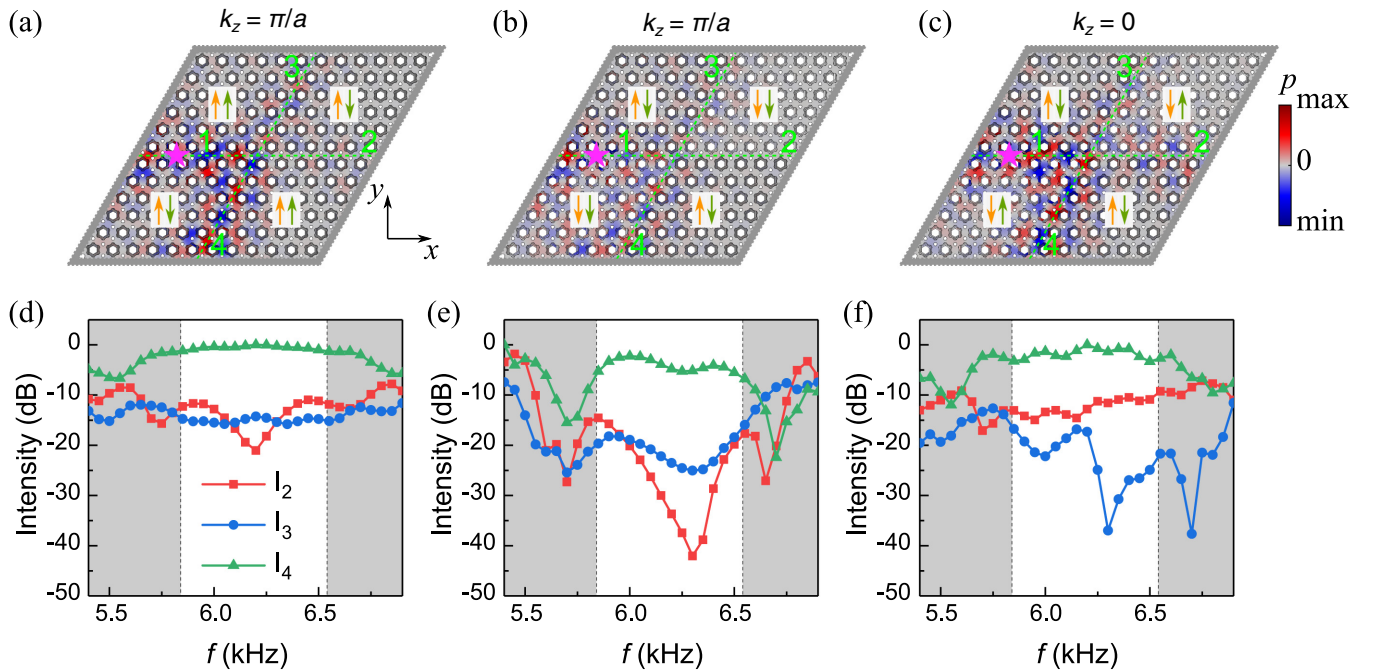
FIG. 4. (a)–(c) Pressure field distribution in the X-shaped cross waveguides. Interfaces are formed by four different domains, where orange up and down arrows represent interlayer hopping strengths $|t_{c1}| > |t_{c2}|$ and $|t_{c1}| < |t_{c2}|$. Green arrows represent the chiralities of the interlayer hopping. The waveguide is periodic in the z direction. The purple star is the location of the monopole acoustic source. The waveguide is surrounded by absorbent materials. (d)–(f) Corresponding normalized acoustic intensity at the exits of the waveguide.

shown in Figs. 3(f) and 3(i). The crossing of the interface band at $k_z = 0$ is caused by inversion of the layer pseudospin sectors. The band inversion does not happen at $k_z = 0$ but at H in the BZ. The interface Dirac cones are distinguished from the quasi-1D Dirac dispersion [35]. The dispersion near Dirac cones is equivalent to a 2D Dirac particle, while the quasi-1D Dirac dispersion is approximately equal to a 1D Dirac particle at each k_z. Only the quasi-1D Dirac dispersion has separate pseudospin-polarized sectors.

IV. X-SHAPED WAVEGUIDES

X-shaped waveguides are commonly used to check the pseudospin-dependent transport properties in classical systems [7]. X-shaped interfaces in three dimensional are a more interesting phenomenon because the dispersion or the mechanism of the interface states is richer than in 2D conditions. Based on the three different types of interfaces depicted in Figs. 3(a)–3(c), we designed X-shaped cross waveguides to study the partition behavior of interface states. The simulated pressure field is shown in Figs. 4(a)–4(c) with certain k_z. The incident acoustic wave from interface 1 tends to transmit through a sharp angle to interface 4 since the interface modes between interfaces 1 and 4 overlap better. The transmission to interface 2 is forbidden if interfaces are formed by band inversion [Fig. 4(b)], which is similar to 2D acoustic topological insulators. The intensity of the acoustic wave at the exits of interface 2 is comparatively low, as shown in Fig. 4(e). For interfaces formed by inversion of layer pseudospin sectors, the lack of spin conservation results in the pseudospin flipping in the cross waveguide [9]. The interface states not

only can propagate to interfaces 3 and 4 with the same layer pseudospin polarization $\langle \sigma_y \rangle$ but also can transport to interface 2 with pseudospin flipping, as shown in Figs. 4(d) and 4(f). The result for a specific k_z in Fig. 4 can be achieved using the experimental procedure in two different ways. One can extract different k_z components by Fourier transforming the field distribution or using a sound source array to stimulate the specific k_z component.

The surface and interface states allow us to design a surface-interface-surface waveguide. Combining the surface and interface states, the acoustic wave propagation path can be tailored in various ways. In Figs. 5(a) and 5(b), we illustrate equifrequency contour (EFC) analysis for surface-interface-surface acoustic beam propagation [22]. The layer-pseudospin-polarized surface or interface states lack diffraction along the z direction because the EFCs are almost flat [Fig. 5(a)]. When the interface states are not layer pseudospin polarized [Fig. 5(b)], the acoustic beam is expanded in the interface region because of the circular EFC in the Dirac cone dispersion. In Fig. 5(c), the X-shaped waveguide is composed of two acoustic domains, where the chirality in one of the domains is inverted. Interface waves and surface waves are both layer pseudospin polarized. The surface wave transport is clockwise in the left domain and becomes counterclockwise in the right domain. Here, the transmission to terminal 2 is forbidden. The acoustic beam is not expanded across the interface. A dominant ratio of acoustic waves can be transported to terminal 3, as shown in Fig. 5(d). If the interface states are not layer pseudospin polarized, we observe transmission to both terminals 2 and 3, as shown in Figs. 5(e)–5(h), which means the incident wave is converted
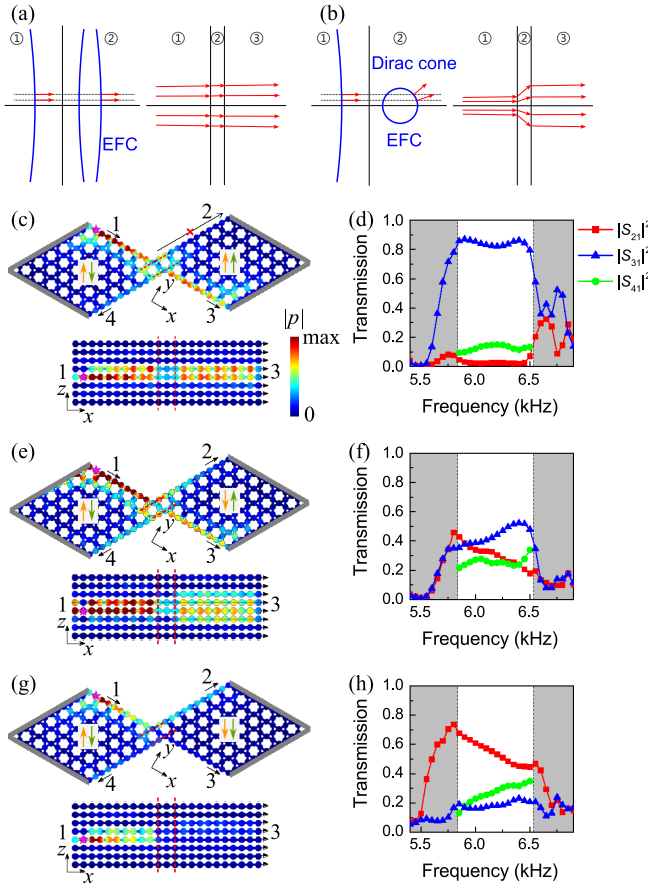
FIG. 5. (a) and (b) Schematic of equifrequency contour (EFC) analyses (left panel) for surface-interface-surface acoustic beam propagation (right panel). The surface, interface, and surface regions are denoted by circled 1, 2, and 3. The interface states in (a) are layer pseudospin polarized and have a crossing dispersion, while the interface in (b) has a Dirac cone dispersion. (c), (e), and (g) Pressure field distribution of the surface wave in the x-y (top) and x-z (bottom) cut planes at 6.2 kHz. The X-shaped waveguide is composed of two different domains with inversion of the (c) pseudospin sectors, (e) pseudospin sectors and bands, or (g) only the bands. The structure is constructed by stacking double-diamond elements along z. The waveguide ends with absorbent materials. The pink star denotes the position of the source. (d), (f), and (h) Corresponding transmission from surface 1 to terminal surfaces 2, 3, and 4. S_{ij} are the S parameters of the waveguide.

into two layer-pseudospin sectors. The interface also acts as a beam expander of the directional surface wave, as shown in the x-z cut plane in Fig. 5(e). For the X-shaped waveguide formed by band inversion in Fig. 5(g), the transmission to terminal 2 is dominant because the pseudospin sectors are not inverted [Fig. 5(h)]. For a case between Figs. 5(c) and 5(g), in which the waveguide is formed by inversion of both pseudospins and bands, neither the transmission to terminal 2 nor that to terminal 3 is dominant [Fig. 5(f)]. By combining the surface and interface states, the acoustic wave propagation in the band gap can be tailored in more flexible and diverse ways. Applications such as pseudospin converters and beam splitters may have potential value in innovative acoustic devices.

V. CONCLUSIONS

In conclusion, we have experimentally realized an acoustic fragile topological insulator, in which topological surface states in three different surfaces are observed. Topological interface states are found at the domain walls where inversion of pseudospin sectors or bands is introduced. The transport behavior of surface and interface states in X-shaped waveguide become much complex than in the 2D case because of the richer topological properties. The system provides a platform to investigate applications implementing both surface states and interface states, such as focusing, sensing, and waveguiding. The breathing kagome lattice can further be utilized to realize higher-order 3D topological insulators [36–40].

APPENDIX A: TIGHT-BINDING MODEL AND SYMMETRY ANALYSES

In this Appendix, we summarize how the interface and surface states arise from the bulk topology. The surface states stem from the fragile topology and the polarization of pseudospin sectors for bands below the gap. The interface states with cone dispersion stem from the band inversion when exchanging interlayer hopping strengths t_{c1} and t_{c2}. These two different mechanisms allowed us to design various kinds of waveguides in the main text.

1. Tight-binding model

We introduce a tight-binding model that includes interatomic hopping between intralayer nearest neighbors and interlayer next-nearest neighbors. The tight-binding Hamiltonian in real space is

$$H = \sum_i \varepsilon_i c_i^\dagger c_i + t_1 \sum_{\langle ij \rangle} c_i^\dagger c_j$$
$$+ \sum_{\langle\langle ij \rangle\rangle, \alpha} [t_{c1} v_{ij,\alpha} c_{i,\alpha}^\dagger c_{j,\alpha+1} + t_{c2} v_{ij,\alpha} c_{i,\alpha}^\dagger c_{j,\alpha-1} + \text{H.c.}],$$

(A1)

where c and $c^\dagger$ are the annihilation and creation operators on the sublattice sites and the subscripts (i, j) represent the lattice sites of each layer. The first term represents the on-site energy. The second term represents hopping between intralayer nearest neighbors with strength t_1. The last term is the chiral interlayer hopping between the next-nearest neighbors, where t_{c1} and t_{c2} are the hopping strengths and α represents layers with odd numbers. $v_{ij,\alpha} = [(2/\sqrt{3})(\hat{\mathbf{e}}_{ij,\alpha}^1 \times \hat{\mathbf{e}}_{ij,\alpha}^2)_z + 1]/2$

encodes the chirality of the interlayer hopping, where $\hat{\mathbf{e}}_{ij,\alpha}^{1,2}$ are the two nearest-neighbor bond unit vectors traversed between sites i and j. The Bloch Hamiltonian can be written as

$$H(\mathbf{k}) = \begin{pmatrix} H_1 & H_2 \\ H_2^\dagger & H_1 \end{pmatrix}, \qquad (A2)$$

where

$$H_1 = 2t_1 \begin{pmatrix} 0 & \cos(\mathbf{k} \cdot \mathbf{a}_3) & \cos(\mathbf{k} \cdot \mathbf{a}_2) \\ \cos(\mathbf{k} \cdot \mathbf{a}_3) & 0 & \cos(\mathbf{k} \cdot \mathbf{a}_1) \\ \cos(\mathbf{k} \cdot \mathbf{a}_2) & \cos(\mathbf{k} \cdot \mathbf{a}_1) & 0 \end{pmatrix} \qquad (A3)$$

and

$$H_2 = 2(t_{c1}e^{\frac{ik_z a}{2}} + t_{c2}e^{-\frac{ik_z a}{2}})$$
$$\times \begin{pmatrix} 0 & 0 & \cos(\mathbf{k} \cdot \mathbf{a}_2') \\ \cos(\mathbf{k} \cdot \mathbf{a}_3') & 0 & 0 \\ 0 & \cos(\mathbf{k} \cdot \mathbf{a}_1') & 0 \end{pmatrix}. \qquad (A4)$$

$\mathbf{a}_i$ and $\mathbf{a}_i'$ ($i = 1, 2, 3$) are the nearest and next-nearest hopping vectors of the kagome lattice, where $\mathbf{a}_1 = (-a/4, \sqrt{3}a/4, 0)$, $\mathbf{a}_2 = (-a/4, -\sqrt{3}a/4, 0)$, $\mathbf{a}_3 = (a/2, 0, 0)$, $\mathbf{a}_1' = (-3a/4, -\sqrt{3}a/4, 0)$, $\mathbf{a}_2' = (3a/4, -\sqrt{3}a/4, 0)$, and $\mathbf{a}_3' = (0, \sqrt{3}a/2, 0)$. The basis of the Hamiltonian is $\phi e^{i\mathbf{k} \cdot \mathbf{r}}$, which is a Bloch eigenstate ϕ with a phase factor. The Hamiltonian can be written in Gell-Mann matrix form as

$$H(\mathbf{k}) = 2t_1\sigma_0 \mathbf{d_k} \cdot \mathbf{S}$$
$$+ \cos(k_z a/2)(t_{c1} + t_{c2})(\sigma_x \mathbf{d_k'} \cdot \mathbf{S} + \sigma_y \mathbf{d_k'} \cdot \mathbf{S'})$$
$$+ \sin(k_z a/2)(t_{c1} - t_{c2})(\sigma_y \mathbf{d_k'} \cdot \mathbf{S} - \sigma_x \mathbf{d_k'} \cdot \mathbf{S'}), \quad (A5)$$

where $\mathbf{d_k} = (\cos(\mathbf{k} \cdot \mathbf{a}_1), \cos(\mathbf{k} \cdot \mathbf{a}_2), \cos(\mathbf{k} \cdot \mathbf{a}_3))$, $\mathbf{d_k'} = (\cos(\mathbf{k} \cdot \mathbf{a}_1'), \cos(\mathbf{k} \cdot \mathbf{a}_2'), \cos(\mathbf{k} \cdot \mathbf{a}_3'))$, $\mathbf{S} = (\lambda_6, \lambda_4, \lambda_1)$, and $\mathbf{S'} = (\lambda_7, -\lambda_5, \lambda_2)$. λ_i ($i = 1, \ldots, 8$) are the Gell-Mann matrices acting on the sublattice pseudospins. $\sigma = (\sigma_x, \sigma_y, \sigma_z, \sigma_0)$ are the Pauli matrices for layer pseudospins. When $t_{c1} = t_{c2}$, the Hamiltonian reduces to a Dirac Hamiltonian in the $k_z = \pi/a$ plane, where a fourfold Dirac point appears at the H point in the BZ.

2. Fragile topology and layer-pseudospin-polarized transport

Here, we present the matrix representation of the rotation symmetries. The rotational axis is site $1a$ of the unit cell.

$$c_6 = \sigma_0 \otimes \begin{pmatrix} 0 & 0 & e^{-i(k_x/4+\sqrt{3}k_y/4)} \\ e^{-ik_x/2} & 0 & 0 \\ 0 & e^{-i(k_x/4+\sqrt{3}k_y/4)} & 0 \end{pmatrix}, \qquad (A6)$$

$$c_3 = \sigma_0 \otimes \begin{pmatrix} 0 & e^{-i\sqrt{3}k_y/2} & 0 \\ 0 & 0 & e^{-i(3k_x/4+\sqrt{3}k_y/4)} \\ e^{-i(3k_x/4-\sqrt{3}k_y/4)} & 0 & 0 \end{pmatrix}, \qquad (A7)$$

$$c_2 = \sigma_0 \otimes \begin{pmatrix} e^{i(k_x/2-\sqrt{3}k_y/2)} & 0 & 0 \\ 0 & e^{-i(k_x/2+\sqrt{3}k_y/2)} & 0 \\ 0 & 0 & e^{-ik_x} \end{pmatrix}. \qquad (A8)$$
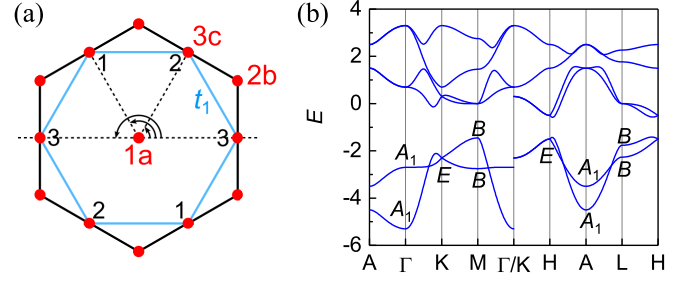

FIG. 6. (a) Symmetries of the tight-binding model. The locations and labels of the maximal Wyckoff positions are in red. t_1 is the nearest-neighboring hopping. (b) Band structures of the tight-binding model with $t_1 = -1, t_{c1} = -0.45, t_{c2} = -0.2$. Little group representations are labeled for the lower two bands.

We calculate the tight-binding band structure and label the high-symmetry points in Fig. 6. The corresponding irreducible representations are given in Table I. The topology of a gapped band structure is characterized by the symmetry data vector $B = \sum_i p_i \text{EBR}_i$, which is a linear combination of elementary band representations (EBRs) [19]. A complete list of the spinless EBRs for $p6$ with time-reversal symmetry and without spin-obit coupling is presented in Table II. The lowest two bands have the missing EBR induced by the Wyckoff position, which is a characteristic of a fragile topological insulator. For example, one decomposition of the lowest two bands is

$$(A)_{1a} \oplus \left(^1E_2{}^2E_2\right)_{1a} \oplus (A)_{2b} \ominus (B)_{3c}. \qquad (A9)$$

TABLE I. Character tables for $p6$ and the relevant little groups. The first column gives the standard name according to Altmann-Herzig notation (AH). The second column gives another name at the high-symmetry points in the Brillouin zone according to the Bilbao Crystallographic Server (BCS).

PG 6					
AH	BCS	E	c_6	c_3	c_2
A	Γ_1, A_1	1	1	1	1
B	Γ_2, A_2	1	-1	1	-1
$^1E_1$	Γ_6, A_6	1	$e^{-i\frac{\pi}{3}}$	$e^{-i\frac{2\pi}{3}}$	-1
$^2E_1$	Γ_4, A_4	1	$e^{i\frac{\pi}{3}}$	$e^{i\frac{2\pi}{3}}$	-1
$^1E_2$	Γ_5, A_5	1	$e^{i\frac{2\pi}{3}}$	$e^{i\frac{4\pi}{3}}$	1
$^2E_2$	Γ_3, A_3	1	$e^{-i\frac{2\pi}{3}}$	$e^{-i\frac{4\pi}{3}}$	1
PG 3					
AH	BCS	E		c_3	
A	K_1, H_1	1		1	
^1E	K_2, H_2	1		$e^{i\frac{2\pi}{3}}$	
^2E	K_3, H_3	1		$e^{-i\frac{2\pi}{3}}$	
PG 2					
AH	BCS	E		c_2	
A	M_1, L_1	1		1	
B	M_2, L_2	1		-1	

TABLE II. Elementary band representations (EBRs) for $p6$. The columns denote the EBR as $(R)_l$. R is the irreducible representation of the orbital that induces the EBR. l denotes the maximal Wyckoff position where the orbital locates. The last row is the decomposition coefficient p_i for each EBR in the acoustic topological insulator, where $a, b \in \mathbb{Z}$.

	Band representation							
	$(A)_{1a}$	$(B)_{1a}$	$(^1E_1{}^2E_1)_{1a}$	$(^1E_2{}^2E_2)_{1a}$	$(A)_{2b}$	$(^1E^2E)_{1a}$	$(A)_{3c}$	$(B)_{3c}$
A	A_1	A_2	A_3A_5	A_4A_6	$A_1 \oplus A_2$	$A_3A_5 \oplus A_4A_6$	$A_1 \oplus A_3A_5$	$A_2 \oplus A_4A_6$
Γ	Γ_1	Γ_2	$\Gamma_3\Gamma_5$	$\Gamma_4\Gamma_6$	$\Gamma_1 \oplus \Gamma_2$	$\Gamma_3\Gamma_5 \oplus \Gamma_4\Gamma_6$	$\Gamma_1 \oplus \Gamma_3\Gamma_5$	$\Gamma_2 \oplus \Gamma_4\Gamma_6$
H	H_1	H_1	H_2H_3	H_2H_3	H_2H_3	$2H_1 \oplus H_2H_3$	$H_1 \oplus H_2H_3$	$H_1 \oplus H_2H_3$
K	K_1	K_1	K_2K_3	K_2K_3	K_2K_3	$2K_1 \oplus K_2K_3$	$K_1 \oplus K_2K_3$	$K_1 \oplus K_2K_3$
L	L_1	L_2	$2L_1$	$2L_2$	$L_1 \oplus L_2$	$2L_1 \oplus 2L_2$	$L_1 \oplus 2L_2$	$2L_1 \oplus L_2$
M	M_1	M_2	$2M_1$	$2M_2$	$M_1 \oplus M_2$	$2M_1 \oplus 2M_2$	$M_1 \oplus 2M_2$	$2M_1 \oplus M_2$
p_i	a	$a-1$	$a-1$	a	b	$b-1$	$2-a-b$	$1-a-b$

The decomposition is always a difference of EBRs, which indicates the fragile topology of the acoustic crystal.

The evolution of the Wannier charge centers (WCCs) in the lowest two bands is calculated with the simulated eigenstates, as shown in Fig. 7. The evolution of WCCs below the band gap shows a nontrivial winding number in the $k_z = 0$ and $k_z = \pi/a$ planes. For each k_z, the nontrivial winding of WCCs gives rise to a pseudospin-polarized surface wave transport. The calculation of WCCs is also performed in planes parallel to the k_z axis. The winding of WCCs in planes $k_{1,2} = 0$ and $k_{1,2} = \pi/a$ is trivial.

Similar to the spin-Chern insulator, the bands below the gap can be projected into layer pseudospin sectors with an open spin gap. The projected Hamiltonian H_s in the layer pseudospin space is

$$H_s = \begin{pmatrix} \langle\phi_1|\tau_y|\phi_1\rangle & \langle\phi_1|\tau_y|\phi_2\rangle \\ \langle\phi_2|\tau_y|\phi_1\rangle & \langle\phi_2|\tau_y|\phi_2\rangle \end{pmatrix}, \quad (A10)$$

where ϕ_1 and ϕ_2 are the Bloch wave functions of the lower two bands, $\tau_y = \sigma_y \otimes \mathbb{I}_{3\times3}$. We obtain two pseudospin bands with gapped eigenvalues $\chi_\pm$ and eigenvectors $\psi_\pm = (\alpha_\pm, \beta_\pm)$. The lowest two bands can be projected into two spin sectors as

$$\phi_\pm = \alpha_\pm\phi_1 + \beta_\pm\phi_2. \quad (A11)$$

Each spin sector has a pseudospin-polarized Chern number in each k_z,

$$C_\pm(k_z) = \frac{1}{2\pi}\int_{BZ} dk_x dk_y \Omega_\pm, \quad (A12)$$

where $\Omega_\pm = \hat{\mathbf{e}}_z \cdot [\nabla_{\mathbf{k}} \times \langle\phi_\pm|i\nabla_{\mathbf{k}}|\phi_\pm\rangle]$ are the Berry curvatures. We have a pair of nontrivial pseudospin-polarized Chern numbers $C_\pm = \pm1$ or a spin-Chern number $C_s = (C_+ - C_-)/2 = 1$ for the lowest two bands. When the chirality of the interlayer hopping is inverted, the pseudospin-polarized Chern numbers change sign, that is, $C_\pm = \mp1$ and $C_s = -1$.

Accordingly, the pseudospins up and down for surface states can be defined by the projection on σ_y. The pseudospin polarization for the surface state is defined as $\langle\sigma_y\rangle = \langle\phi_{\mathbf{k}}|\sigma_y|\phi_{\mathbf{k}}\rangle$. We obtain two branches of surface states with pseudospin-momentum locking in the main text.

3. Interface states with band inversion

The mechanism of interface Dirac cones differs from the layer-pseudospin-polarized states, as the interface Dirac cones are achieved through band inversion. Using $\mathbf{k} \cdot \mathbf{P}$ perturbation theory, we evaluate the effective model near the H point in the BZ. The lowest four eigenstates at the H point are

$$\phi_1 = \frac{1}{\sqrt{6}}\big(e^{i\frac{2\pi}{3}}, e^{i\frac{2\pi}{3}}, 1, e^{i\frac{4\pi}{3}}, e^{i\frac{4\pi}{3}}, e^{i\frac{2\pi}{3}}\big)^T,$$

$$\phi_2 = \frac{1}{\sqrt{6}}\big(e^{i\frac{4\pi}{3}}, 1, 1, e^{i\frac{2\pi}{3}}, e^{i\frac{4\pi}{3}}, e^{i\frac{4\pi}{3}}\big)^T,$$

$$\phi_3 = \frac{1}{\sqrt{6}}\big(e^{i\frac{5\pi}{3}}, e^{i\frac{5\pi}{3}}, -1, e^{i\frac{4\pi}{3}}, e^{i\frac{4\pi}{3}}, e^{i\frac{2\pi}{3}}\big)^T,$$

$$\phi_4 = \frac{1}{\sqrt{6}}\big(e^{i\frac{\pi}{3}}, -1, -1, e^{i\frac{2\pi}{3}}, e^{i\frac{4\pi}{3}}, e^{i\frac{4\pi}{3}}\big)^T. \quad (A13)$$

Cavities linked by t_{c1} are in phase coupled for $\phi_{1,2}$ and out of phase coupled for $\phi_{3,4}$. $\phi_{1,3}$ and $\phi_{2,4}$ carry orbital angular momenta -1 and $+1$ along the z direction, respectively. The simulated results of eigenstates are shown in Fig. 8, which is in agreement with the tight-binding model. In the basis of $(\phi_1, \phi_2, \phi_3, \phi_4)$, the effective Hamiltonian near the H point up
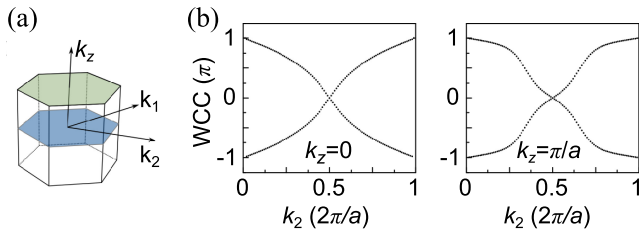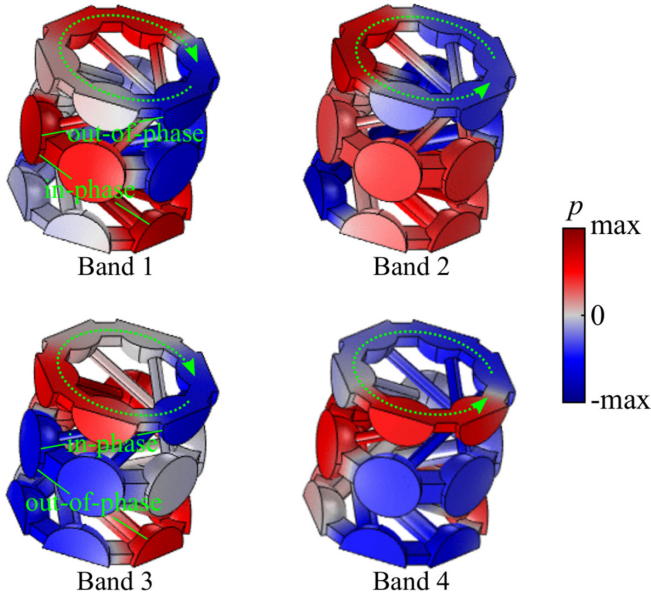

FIG. 7. (a) BZ with reciprocal lattice vectors in the k_1, k_2, and k_z directions. (b) Evolution of the Wannier charge center (WCC) along the k_2 direction for the lowest two bands. The WCC is calculated using the Wilson loop method in the k_1 direction.

FIG. 8. Simulated pressure field profile of eigenstates near the H point of the BZ. The pressure eigenstates of band i ($i \in 1, 2, 3, 4$) correspond to the Bloch eigenstates ϕ_i in the tight-binding model.

to the linear term is

$$H_{\text{eff}} = \begin{pmatrix} t_1 + m & \alpha k_+ & -i\gamma\delta k_z & \beta k_+ \\ \alpha^* k_- & t_1 + m & \beta^* k_- & -i\gamma\delta k_z \\ i\gamma\delta k_z & \beta k_+ & t_1 - m & \alpha k_+ \\ \beta^* k_- & i\gamma\delta k_z & \alpha^* k_- & t_1 - m \end{pmatrix}, \quad (A14)$$

where $m = 2(t_{c1} - t_{c2})$ is the effective mass induced by the breaking of mirror symmetry. Other parameters are $k_\pm = \delta k_x \pm i\delta k_y$, $\alpha = (\sqrt{3}t_1/4)e^{i4\pi/3}$, $\beta = (3t_1/4)e^{-i\pi/6}$, and $\gamma = t_{c1} + t_{c2}$. The $m\sigma_z$ term lifts the degeneracy of the 3D Dirac point. When the sign of the mass term is reversed $m \to -m$, the band inversion occurs. A 2D topological domain wall separating 3D structures with opposite signs for the effective mass m should host topological surface states exhibiting linear 2D Dirac-like dispersion at the projection of the H point in the surface BZ [31], which is shown in Fig. 3(c).

APPENDIX B: SURFACE STATES IN THE YZ AND TOP XY SURFACES

The YZ surface has a zigzag whole-cell boundary, as shown in Fig. 9(a). The spatial fields in Fig. 9(b) show the propagating acoustic wave measured at 6.2 kHz. The surface wave distribution at the YZ surface is similar to that at the XZ surface. The measured band dispersions at the YZ surface are shown in Fig. 9(c). Two branches of surface band dispersion cross at $\bar{\Gamma}\bar{Z}$ in the surface BZ for higher frequencies, forming a tiny gap because of the lack of glide reflection symmetries. The equifrequency contours on the YZ surface also demonstrate crossing of surface bands at higher frequencies, as shown in Fig. 9(d).

The top and bottom surfaces of the weak topological insulator are usually trivial, and no surface states are found. However, the weakly coupled surface layer in the acoustic crystal can be utilized to achieve a surface Dirac cone in
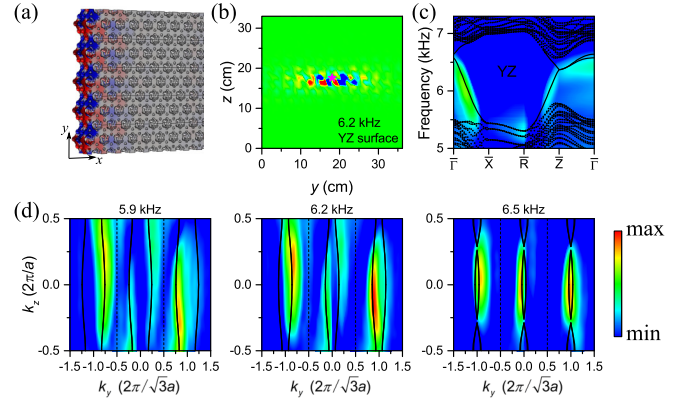

FIG. 9. (a) Pressure field distribution of the topological surface state on the (a) YZ (100) surface with a flat boundary. (b) Measured real-space propagation of a surface wave excited by a pointlike source. (c) Surface band dispersion on the YZ surface. (d) Equifrequency contours of the surface state at 5.9, 6.2, and 6.5 kHz. The color bar in (c) and (d) denotes the magnitude of the spatial Fourier transformation. The solid black lines and dots denote the simulation results. The dashed black lines denote the boundary of the first BZ.

the band gap. The top and bottom surfaces have a half-cell boundary, as shown in Fig. 10(a), where the weakly (strongly) coupled layer is at the top (bottom). The cut planes of the half-cell boundaries for the top and bottom surfaces are mirror planes in the structure. The spatial field at the top surface shows a ring pattern and transport in all directions, as shown in Fig. 10(b). In contrast to the side surfaces, the XY surface supports a surface Dirac cone protected by the rotational symmetry and a nontrivial Zak phase, as shown in Fig. 10(c). The weakly coupled layer at the top surface acts as a 2D hexagonal acoustic semimetal. If the surface layer has strong coupling to the bulk, then the surface states will vanish as the strongly coupled layers become similar to a bilayer spin-Chern insulator [9]. The half-cell boundary can be viewed as a mirror plane, which is equivalent to an interface with a weakly coupled whole-cell layer.
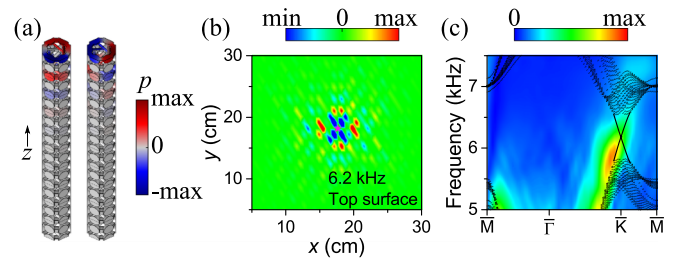

FIG. 10. (a) Bloch field distributions for surface states of the top surface with a half-cell boundary. The pillarlike structure contains 10 unit cells stacked along the z direction. The structure has periodic boundary conditions in directions perpendicular to the z direction, while the top and bottom are hard boundaries. (b) Measured real-space propagation of a surface wave excited by a pointlike source. (c) Measured surface band dispersion on the top surface (color map) in contrast to the simulation. The color bar in (c) denotes the magnitude of the spatial Fourier transformation.

[1] A. B. Khanikaev, S. H. Mousavi, W.-K. Tse, M. Kargarian, A. H. MacDonald, and G. Shvets, Photonic topological insulators, Nat. Mater. **12**, 233 (2013).

[2] L.-H. Wu and X. Hu, Scheme for Achieving a Topological Photonic Crystal by Using Dielectric Material, Phys. Rev. Lett. **114**, 223901 (2015).

[3] M. C. Rechtsman, J. M. Zeuner, Y. Plotnik, Y. Lumer, D. Podolsky, F. Dreisow, S. Nolte, M. Segev, and A. Szameit, Photonic Floquet topological insulators, Nature (London) **496**, 196 (2013).

[4] L. Lu, J. D. Joannopoulos, and M. Soljačić, Topological photonics, Nat. Photonics **8**, 821 (2014).

[5] T. Ozawa, H. M. Price, A. Amo, N. Goldman, M. Hafezi, L. Lu, M. C. Rechtsman, D. Schuster, J. Simon, O. Zilberberg, and I. Carusotto, Topological photonics, Rev. Mod. Phys. **91**, 015006 (2019).

[6] M. Kim, Z. Jacob, and J. Rho, Recent advances in 2D, 3D and higher-order topological photonics, Light: Sci. Appl. **9**, 130 (2020).

[7] C. He, X. Ni, H. Ge, X.-C. Sun, Y.-B. Chen, M.-H. Lu, X.-P. Liu, and Y.-F. Chen, Acoustic topological insulator and robust one-way sound transport, Nat. Phys. **12**, 1124 (2016).

[8] R. Fleury, A. B. Khanikaev, and A. Alù, Floquet topological insulators for sound, Nat. Commun. **7**, 11744 (2016).

[9] W. Deng, X. Huang, J. Lu, V. Peri, F. Li, S. D. Huber, and Z. Liu, Acoustic spin-Chern insulator induced by synthetic spin–orbit coupling with spin conservation breaking, Nat. Commun. **11**, 3227 (2020).

[10] X. Zhang, M. Xiao, Y. Cheng, M.-H. Lu, and J. Christensen, Topological sound, Commun. Phys. **1**, 97 (2018).

[11] S. H. Mousavi, A. B. Khanikaev, and Z. Wang, Topologically protected elastic waves in phononic metamaterials, Nat. Commun. **6**, 8682 (2015).

[12] A. Foehr, O. R. Bilal, S. D. Huber, and C. Daraio, Spiral-Based Phononic Plates: From Wave Beaming to Topological Insulators, Phys. Rev. Lett. **120**, 205501 (2018).

[13] M. A. Bandres, S. Wittek, G. Harari, M. Parto, J. Ren, M. Segev, D. N. Christodoulides, and M. Khajavikhan, Topological insulator laser: Experiments, Science **359**, eaar4005 (2018).

[14] B. Xie, H. Liu, H. Cheng, Z. Liu, S. Chen, and J. Tian, Acoustic Topological Transport and Refraction in a Kekulé Lattice, Phys. Rev. Appl. **11**, 044086 (2019).

[15] Z. Zhang, Q. Wei, Y. Cheng, T. Zhang, D. Wu, and X. Liu, Topological Creation of Acoustic Pseudospin Multipoles in a Flow-Free Symmetry-Broken Metamaterial Lattice, Phys. Rev. Lett. **118**, 084303 (2017).

[16] Y.-G. Peng, C.-Z. Qin, D.-G. Zhao, Y.-X. Shen, X.-Y. Xu, M. Bao, H. Jia, and X.-F. Zhu, Experimental demonstration of anomalous Floquet topological insulator for sound, Nat. Commun. **7**, 13368 (2016).

[17] Y. Yang, J. Lu, M. Yan, X. Huang, W. Deng, and Z. Liu, Hybrid-Order Topological Insulators in a Phononic Crystal, Phys. Rev. Lett. **126**, 156801 (2021).

[18] V. Peri, Z.-D. Song, M. Serra-Garcia, P. Engeler, R. Queiroz, X. Huang, W. Deng, Z. Liu, B. A. Bernevig, and S. D. Huber, Experimental characterization of fragile topology in an acoustic metamaterial, Science **367**, 797 (2020).

[19] B. Bradlyn, L. Elcoro, J. Cano, M. G. Vergniory, Z. Wang, C. Felser, M. I. Aroyo, and B. A. Bernevig, Topological quantum chemistry, Nature (London) **547**, 298 (2017).

[20] F. Li, X. Huang, J. Lu, J. Ma, and Z. Liu, Weyl points and Fermi arcs in a chiral phononic crystal, Nat. Phys. **14**, 30 (2018).

[21] B. Xie, H. Liu, H. Cheng, Z. Liu, S. Chen, and J. Tian, Experimental Realization of Type-II Weyl Points and Fermi Arcs in Phononic Crystal, Phys. Rev. Lett. **122**, 104302 (2019).

[22] H. He, C. Qiu, L. Ye, X. Cai, X. Fan, M. Ke, F. Zhang, and Z. Liu, Topological negative refraction of surface acoustic waves in a Weyl phononic crystal, Nature (London) **560**, 61 (2018).

[23] X. Cai, L. Ye, C. Qiu, M. Xiao, R. Yu, M. Ke, and Z. Liu, Symmetry-enforced three-dimensional Dirac phononic crystals, Light: Sci. Appl. **9**, 38 (2020).

[24] B. Xie, H. Liu, H. Cheng, Z. Liu, J. Tian, and S. Chen, Dirac points and the transition towards Weyl points in three-dimensional sonic crystals, Light: Sci. Appl. **9**, 201 (2020).

[25] H. Cheng, Y. Sha, R. Liu, C. Fang, and L. Lu, Discovering Topological Surface States of Dirac Points, Phys. Rev. Lett. **124**, 104301 (2020).

[26] W. Deng, J. Lu, F. Li, X. Huang, M. Yan, J. Ma, and Z. Liu, Nodal rings and drumhead surface states in phononic crystals, Nat. Commun. **10**, 1769 (2019).

[27] H. Qiu, C. Qiu, R. Yu, M. Xiao, H. He, L. Ye, M. Ke, and Z. Liu, Straight nodal lines and waterslide surface states observed in acoustic metacrystals, Phys. Rev. B **100**, 041303(R) (2019).

[28] Y. Yang, J.-P. Xia, H.-X. Sun, Y. Ge, D. Jia, S.-Q. Yuan, S. A. Yang, Y. Chong, and B. Zhang, Observation of a topological nodal surface and its surface-state arcs in an artificial acoustic crystal, Nat. Commun. **10**, 5185 (2019).

[29] C. He, S.-Y. Yu, H. Ge, H. Wang, Y. Tian, H. Zhang, X.-C. Sun, Y. B. Chen, J. Zhou, M.-H. Lu, and Y.-F. Chen, Three-dimensional topological acoustic crystals with pseudospin-valley coupled saddle surface states, Nat. Commun. **9**, 4555 (2018).

[30] C. He, S.-Y. Yu, H. Wang, H. Ge, J. Ruan, H. Zhang, M.-H. Lu, and Y.-F. Chen, Hybrid Acoustic Topological Insulator in Three Dimensions, Phys. Rev. Lett. **123**, 195503 (2019).

[31] A. Slobozhanyuk, S. H. Mousavi, X. Ni, D. Smirnova, Y. S. Kivshar, and A. B. Khanikaev, Three-dimensional all-dielectric photonic topological insulator, Nat. Photonics **11**, 130 (2017).

[32] Y. Yang, Z. Gao, H. Xue, L. Zhang, M. He, Z. Yang, R. Singh, Y. Chong, B. Zhang, and H. Chen, Realization of a three-dimensional photonic topological insulator, Nature (London) **565**, 622 (2019).

[33] C. He, H.-S. Lai, B. He, S.-Y. Yu, X. Xu, M.-H. Lu, and Y.-F. Chen, Acoustic analogues of three-dimensional topological insulators, Nat. Commun. **11**, 2318 (2020).

[34] S. Kobayashi and A. Furusaki, Fragile topological insulators protected by rotation symmetry without spin-orbit coupling, Phys. Rev. B **104**, 195114 (2021).

[35] R. Noguchi *et al.*, A weak topological insulator state in quasi-one-dimensional bismuth iodide, Nature (London) **566**, 518 (2019).

[36] H. Xue, Y. Yang, F. Gao, Y. Chong, and B. Zhang, Acoustic higher-order topological insulator on a kagome lattice, Nat. Mater. **18**, 108 (2019).

[37] H. Xue, Y. Ge, H.-X. Sun, Q. Wang, D. Jia, Y.-J. Guan, S.-Q. Yuan, Y. Chong, and B. Zhang, Observation of an acoustic octupole topological insulator, Nat. Commun. **11**, 2442 (2020).

[38] H. Xue, Y. Yang, G. Liu, F. Gao, Y. Chong, and B. Zhang, Realization of an Acoustic Third-Order Topological Insulator, Phys. Rev. Lett. **122**, 244301 (2019).

[39] X. Ni, M. Li, M. Weiner, A. Alù, and A. B. Khanikaev, Demonstration of a quantized acoustic octupole topological insulator, Nat. Commun. **11**, 2108 (2020).

[40] M. Weiner, X. Ni, M. Li, A. Alù, and A. B. Khanikaev, Demonstration of a third-order hierarchy of topological states in a three-dimensional acoustic metamaterial, Sci. Adv. **6**, eaay4166 (2020).